Thermochimica Acta 486 (2009) 32–40

Contents lists available at ScienceDirect

Thermochimica Acta

journal homepage: www.elsevier.com/locate/tca

Thermodynamic performance analysis and optimization of a SOFC-H$^+$ system

C. Zamfirescu, I. Dincer*

Faculty of Engineering and Applied Science, University of Ontario Institute of Technology (UOIT), 2000 Simcoe Street North, Oshawa, ON, Canada L1H 7K4

ARTICLE INFO

Article history:
Received 16 October 2008
Received in revised form 9 December 2008
Accepted 14 December 2008
Available online 24 December 2008

Keywords:
H-SOFC
Optimization
Thermodynamics
Efficiency
Energy
Exergy
Power density

ABSTRACT

In this paper, we investigate the performance of a newly proposed power and heating system using proton-conducting solid oxide fuel-cell (SOFC-H$^+$) for vehicular applications and its optimization for the best possible performance in terms of power output and efficiency. We also study heat recovery option here to improve the performance. Taking this into account, we calculate the exergy efficiency as 60–75% as a function of the air stoichiometry. Also, we show that by allocating optimal volumes to the main components it is possible to maximize the system's volumetric power output. The optimal allocation is quantified by the ratio of stack's volume versus the overall system volume. Both system configuration and performance depend on the optimization objective that may aim to obtain either maximum power density (or useful space on-board) or maximum efficiency (or driving range). If the optimization is performed for a maximum efficiency, the stack occupies about 75% of the total system volume, but the compactness is reduced by about 40% with respect to the maximum power density design.

1. Introduction

One of the biggest challenges with hydrogen and its use as a fuel in vehicles comes from its low volumetric heat of combustion. This brings a potential problem to fuel-cell vehicles due to storage requirement and space limitation to accommodate a large fuel tank while keeping enough free/useful space on-board. As a consequence, fuel-cell vehicle makers now struggle to reduce the size of the fuel-cell system while maximizing its power generation capacity.

Although proton exchange membrane (PEM) fuel cell is the most preferred and adopted ones for vehicular power generation system, they include several auxiliary equipments such as air compressor, heat exchangers, and a rather large size water management subsystem. Thus, even if they have a relatively compact stack, the space requirement for all plant is still high, as well as the costs, while the life time is rather short [1].

On the contrary, solid oxide fuel cells (SOFC) have not yet been considered a potential option for vehicular applications, although they are characterized by stacks with relatively large size, featuring a less voluminous and more cost effective overall system. Although their high operating temperature is an issue (as commented next), they have some important advantages compared to the PEM systems: (i) they are less expensive and present long life time because no noble metal catalysts are needed for the electrodes [2], (ii) internal reforming of an alternative fuel [3] (e.g., methane [4], syngas [5], methanol [6], ammonia [7], propane [8]) to hydrogen is facilitated so that they can use a reduced size fuel tank, (iii) the exhaust gases posses high exergy which can be converted into additional power [9] and low temperature heating.

One major drawback of SOFC systems that probably impeded their expansion on vehicular applications is represented by their rather long start-up time due to their high operating temperature. It has been suggested that this drawback can be solved by using a SOFC–PEM combination [10]. The heat generated by the SOFC is used for reforming the fuel to be delivered downstream to the PEM. However, as demonstrated in Ref. [10] such a system has a large number of auxiliary components and results in a rather costly, short life time and voluminous solution with respect to the generated power.

As it will be discussed later, the generation of high temperature heat on-board of a vehicle, which is possible with SOFC-H$^+$, brings three key benefits:

- It can drive the reforming reaction of a fuel other than hydrogen.
- It can drive the compressor while expanding hot gases over a turbine.
- It offers cabin heating through heat recovery.

In addition, by applying an on-board absorption cooling, the heat recovery may be used for air-conditioning purposes.

Typically, in SOFCs the oxygen ions (O^{2-}) traverse the electrolyte from cathode to anode where they react with the supplied hydrogen

* Corresponding author.
E-mail addresses: Calin.Zamfirescu@uoit.ca (C. Zamfirescu), Ibrahim.Dincer@uoit.ca (I. Dincer).

0040-6031/$ – see front matter © 2008 Elsevier B.V. All rights reserved.
doi:10.1016/j.tca.2008.12.014

Nomenclature

c	mass concentration (kg/kg)
e	specific exergy (kJ/kg)
$\dot{E}$	exergy rate (W)
f	volume fraction occupied by the stack, Eq. (11)
i	current intensity (A)
h	specific enthalpy (J/kg)
$\dot{m}$	mass flow rate (kg/s)
$\dot{n}$	molar mass flow rate (kmol/s)
$\dot{Q}$	heat rate (W)
R	exergy destruction ratio
S	surface area (m^2)
T	temperature (°C)
US	thermal conductance (W/m^2)
V	voltage, difference of electric potential (V)
$\dot{w}''$	power density (W/m^2)
$\dot{W}$	power (W)

Greek letters

Δ	difference
ε	effectiveness
ϕ	power density of heat exchangers (W/m^3)
λ	stoichiometry
η	efficiency
μ	molecular mass (kg/kmol)
ν	molar concentration (kmol/kmol)
ϑ	volume (m^3)

Superscripts

$''$	per unit of surface (m^2)
$'''$	per unit of volume (m^3)
$\overline{(\,)}$	average value
$\dot{(\,)}$	per unit of time (s)
*	normalized value

Subscripts

c	cell
ch	chemical
cmp	compressor
d	destroyed exergy
e	electrolyte
hx	heat exchangers
L	heat loss through insulation
max	maximum
opt	optimum
s	stoichiometric
T	turbine

to produce water and release the reaction heat. During this process, at the anode, the hydrogen is consumed and water generated, and because of this fact the hydrogen's partial pressure decreases [11].

As a consequence of the low partial pressure of hydrogen, the reaction kinetics is degraded [12] and the only solution to compensate this effect is to supply hydrogen in excess. The excess hydrogen must be then combusted in an afterburner and the released heat recovered or converted into work by a gas turbine [13,14]. Thus, certain amounts of NO_x are formed during the combustion of hydrogen with air.

Recent advances in SOFC technologies and applications have led to the development of high temperature proton-conducting membranes [15]. They bring the important advantage of letting the protons to migrate from anode to cathode. As a consequence, the water formation reaction occurs at the cathode, in a way similar to that from PEM fuel cells. This type of fuel cell is known as proton-conducting SOFC (as commonly denoted with SOFC-H^+) to distinguish them from the traditional ion conducting SOFC, denoted as SOFC-O^{2-} [16].

Complete hydrogen utilization is therefore possible with direct implication in increasing system's simplicity and compactness by eliminating the need of the afterburner. Moreover, because all the hydrogen is reacted electrochemically at the fuel-cell cathode, practically no NO_x is formed, and thus the fuel-cell emission consists only in steam and nitrogen, i.e., it is clean.

The development of the SOFC-H^+ technology exhibits a real potential to replace or complement PEM-FC in vehicular applications because they are less expensive, more compact, with high power generated per unit of volume and may operate at intermediate temperature (e.g., even 300 °C) which makes possible to achieve an acceptable start-up time.

At present, efforts are worldwide devoted to develop proton-conducting membranes. In this respect barium cerate ($BaCeO_3$)-based materials were identified [15] as excellent solid oxide electrolytes because of their high proton-conducting capability over a wide range of temperatures (300–1000 °C). As explained by Demin and Tsiakaras [17] by letting the protons to diffuse through the electrolyte and the water formation reaction to occur at the cathode, the electromotive force and conversion efficiency of the fuel cell is significantly increased with respect to the SOFC-O^{2-} case.

It is speculated [15] that the governing mechanism of proton conduction is based on the hopping of protons between adjacent oxygen ions that are bounded to the atomic structure of the solid oxide electrolytic membrane. The protons, being extremely small, necessitate reduced activation energy as compared to the case of oxygen ions transport through the most advanced SOFC-O^{2-} membranes like those based on yttrium stabilized zirconium or doped ceria systems [18].

Moreover, the electronic conduction of barium cerate materials is much lower than that of doped ceria under operating conditions, and this explains the superior electromotive force, power output and efficiency obtained with the SOFC-H^{2-} systems [19]. It has been also shown that the proton conduction is enhanced at lower temperatures, e.g., 300 °C [20].

The main problem with barium cerate results from the difficulty to sinter it in the form of a solid membrane [15]. Because of this, Ranran et al. [15] doped the barium cerate with samarium (Sm) and thus succeeded to sinter thin membranes featuring thickness as low as 50 μm and high power densities in the range of 1300–3400 W/m^2.

The current experimental developments regard also the use of various fuels with internal reforming at the anodic side: Jamsak et al. [16] studied ethanol-fuelled H-SOFC, Assabumrungrat et al. [21,22] focused on methanol-fuelled systems and Assabumrungrat et al. [23] on direct ethanol SOFC-H^+, Sangtongkitcharoen et al. [24] on methane reforming, and Maffei et al. [26] focused on direct ammonia SOFC-H^+.

A number of researchers [e.g., 21–24] stated that there is no essential difference among SOFC-H^+ and SOFC-O^{2-} systems as far as internal reforming of methanol, ethanol, or methane is concerned. This is in fact explained by the beneficial presence of steam at the anode of SOFC-O^{2-} that facilitates the reforming process. However, as pointed out by [25], the performance of SOFC-H^+ systems is not affected by the system configuration (external, internal, or direct reforming) as it is the case for SOFC-O^{2-}. Note that these aspects are not relevant for ammonia reforming because in this process there is no need to generate additional steam.

Maffei et al. [26] showed that if the barium cerate electrolyte is doped with some elements like gadolinium (Ga) or praseodymium (Pr) the electronic conductivity of the membrane is diminished with impact in improving further the cell efficiency.

In the open literature, there have been cited only few studies on mathematical modeling of SOFC-H^+ systems: one is attributed to Demin and Tsiakaras [17] that regards the thermodynamic analysis of the overall system, and another is that of Ni et al. [26,27] that includes a heat and mass transfer and electrochemical reaction modeling presented in contrast with the SOFC-O^{2+} counterpart.

The present study proposes in the first part a novel power and heat generation system based on hydrogen-fuelled SOFC-H^+. A brief thermodynamic model is established through energy and exergy analyses. Exergy analysis is now a mature methodology that quantifies the system's inefficiency in terms of exergy destruction, i.e., the degradation of the system ability to perform work with respect to its surroundings [28]. Exergy analysis has been performed in the past on various types of fuel-cell systems, including PEM [29] and SOFC [11,30]. In the next section it is demonstrated the newly proposed optimization principle of the fuel-cell design.

It is important to note that the present optimization study is essentially different than optimization of design conditions for maximal power density presented for example in Ref. [31]. In the present approach we assume the most appropriate operating conditions and optimize the configuration of the system comprising the fuel-cell stack and heat exchangers for power maximization per unit of volume. An alternative optimization objective is also discussed in the paper in regards to maximization of the driving range. Optimization of system configuration under the fixed operating conditions, is emphasized also in Refs. [32,33] where the constructal theory by Bejan has been used for design optimization. Over there the optimization was focused in generation of the flow architecture, which considered the rational distribution of the reactants and products in such a way that the fuel-cell stack efficiency is maximized for given geometric constraints. In the present paper, rather than optimizing the flow configuration, we focus on the optimal ratio between the stack volume and overall system volume. Further analysis includes the influence of various parameters on the system configuration and a comparison of two design approaches: design for maximum efficiency or for maximum power density. The theory developed here can also be directly applied to optimize the microproton-exchange-membrane fuel cells [34], treated as a cutting-edge technology which essentially requires a system design optimization for constrained volume. The exergy destroyed for each component of the optimized system is presented as well as its exergy efficiency in two cases, namely, with and without heat recovery of exhaust gases. Some final remarks summarize the main findings and comment on the future perspectives of the topic.

2. Analysis and modeling of the proposed system

In this study, we propose a hydrogen-fuelled SOFC-H^+ system, as illustrated in Fig. 1, comprising the SOFC-H^+ stack, a turbo-charger, four compact heat exchangers, a fuel tank and a pressure regulating device. A hydrogen storage tank with metal hydrides is used in this work to provide hydrogen at about 14 bar pressure at #11. After the pressure regulator, the hydrogen is supplied to the power generation system at #12, and is preheated in two steps through #12–13 and #13–14.

Air taken from the surroundings at #1 is compressed in the charger, delivered to the air-preheater at #2, and then to the fuel-cell stack at #3. The exhaust of the fuel-cell which consists of depleted air and steam is directed toward the turbine inlet at #4 and expanded with work recovery up to state #5. The hot exhaust at #5 is used to preheat the two reactants: air (#7–8) and hydrogen (#6–8, #8–9), and then either released to the ambient or used for heat recovery in an additional heat exchanger (#9–10).

The conceptual design is made in such a way that the two reacting streams, prior to be supplied to the fuel-cell stack, are preheated

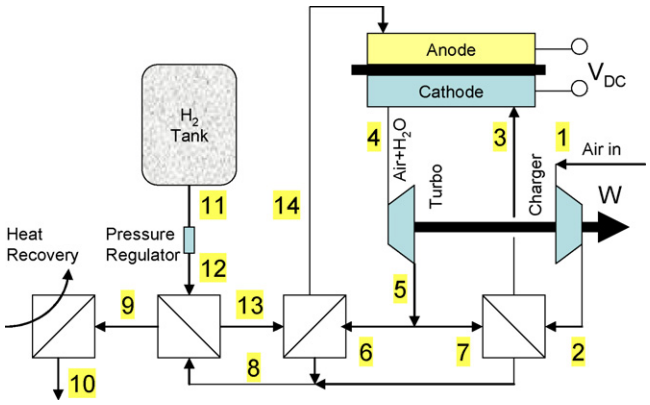

Fig. 1. The proposed SOFC-H^+ system.

to the same temperature in an equal number of two steps. In fact, the air temperature at #2 is same as the hydrogen temperature at #13, and the air temperature at #3 is same as the hydrogen temperature at #14.

Since the fuel-cell considered here is a proton exchange type, some basic modeling equations relating current density to hydrogen and oxygen consumption, and water formation can be employed as taken from Ref. [35] as summarized in Table 1. The stack is assumed to operate at the optimal current density i''_{opt} and its corresponding maximum power density, $\dot{w}''_{max}$. All of the supplied hydrogen is assumed to be consumed by the reaction. The current generated is proportional to the mass exchange surface of the stack (total membrane surface), S, i.e., $i_{opt} = Si''_{opt}$; and hence the output power is $\dot{W}_{max} = S\dot{w}''_{max}$, respectively.

A calculation scheme, which involves the solution of a set of nonlinear equations and other subsequent calculations, is developed to illustrate the thermodynamic cycle and determine all the state points, as outlined below.

First, we have taken the power density versus current density experimental data available in Ref. [25] and regressed particularly the maxima to come up with some practical correlations for use as follows:

$$w''_{max} = 3.4\bar{T}_e - 1650 \quad (1)$$

and

$$i''_{opt} = 8.5\bar{T}_e - 4340 \quad (2)$$

which are valid for the operating temperature range of the fuel cell (e.g., 550–750 °C).

In fact, both power and current densities increase with temperature as demonstrated through mathematical modeling of electrochemical reaction by Ni et al. [26] and confirmed by experimental data from [25]. The optimization procedure presented here later uses interpolations (1) and (2). However, if abatement from linearity is important for some particular case the linear

Table 1
Equations for fuel-cell modeling.

Parameter	Equation
Stoichiometric oxygen consumption	$\dot{m}_{O_{2s}} = 0.0000000829 i_{opt}$(kg/s)
Number of moles of stoichiometric oxygen	$\dot{n}_{O_{2s}} = \dot{m}_{O_{2s}}/\mu_{O_{2s}}$(kmol/s)
Number of moles of stoichiometric air	$\dot{n}_{Air,s} = \dot{n}_{O_{2s}}/c_{O_2}$(kmol/s)
Mass flow rate of stochiometric air	$\dot{m}_{Air,s} = \dot{n}_{Air,s}\mu_{Air}$(kg/s)
Mass flow rate of air	$\dot{m}_{Air} = \dot{m}_{Air,s}\lambda$(kg/s)
Water consumption	$\dot{m}_{H_2O} = 0.0000000934 i_{opt}$(kg/s)
Hydrogen consumption	$\dot{m}_{H_2} = 0.0000000105 i_{opt}$(kg/s)
Molar flow rate of hydrogen	$\dot{n}_{H_2} = \dot{m}_{H_2}/2$(kmol/s)

Source: Ref. [29].

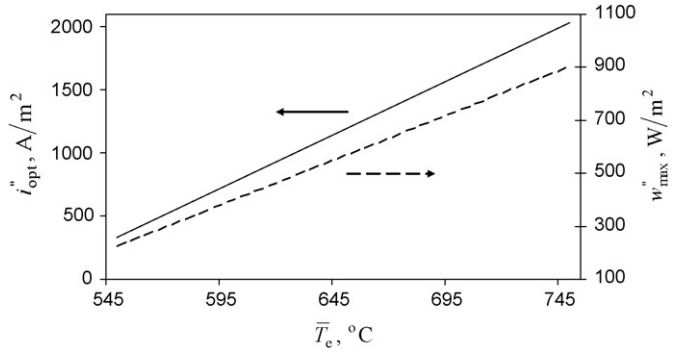

Fig. 2. Optimum current density and maximum power density of the fuel cell [24] in function of the average electrolyte temperature. (a) Variation of the electrolyte temperature. (b) Variation of the power density.

interpolation approach may be kept provided that the performance optimization procedure is repeated a number of times. At each repetition the data for power and current densities is interpolated and Eqs. (1) and (2) generated again, but for a restrained range of cell temperature and hence a better accuracy.

So, we now have the maximum power density and optimum current density as a function of the average temperature of the electrolyte, $\bar{T}_e$. These are plotted in Fig. 2. Note that in the experiments done by Maffei et al. [25] a relatively thick membrane is used, and relatively low power densities are obtained. However, as said above, using a thin membrane one can generate higher power densities. Depending on the temperature, the maximum power density and its corresponding optimal current, as described by the above equations, the present solution scheme will work in the same way.

Based on the assumed electrolyte temperature, the maximum power density and optimal current density are calculated using Eqs. (1) and (2), respectively. All other calculations are essentially performed using the equations/correlations as listed in Table 1. Subsequently, the cell voltage is calculated with $V_c = \dot{W}_{max}/i_{opt}$, the cell efficiency with $\eta_C = V_c/1.25$, the heat generated with $\dot{Q}_C = \dot{W}_{max}(1/\eta_C - 1)$ and lastly the heat loss through the stack's insulation with $\dot{Q}_L = US_L(\bar{T}_e - T_1)$.

In order to perform these and the subsequent calculations a series of modeling parameters are assumed to have constant values, as summarized in Table 2. These parameters and their values are set based on some relevant engineering data for fuel-cell systems. They refer to the ambient temperature and pressure, intake air composition, turbo-charger efficiency and operating pressure, hydrogen storage pressure, and the characteristics of the stack's thermal insulation, as well as chemical exergies, respectively.

Table 2
Summary of some parameters used in modeling.

Parameter	Value
T_1	25 °C
P_1	1.01325 bar
ν_{N_2}	0.775 kmol/kmol
e_{ch,N_2}	631.51 kJ/kmol
ν_{O_2}	0.206 kmol/kmol
e_{ch,O_2}	3914.26 kJ/kmol
ν_{H_2O}	0.018 kmol/kmol
e_{ch,H_2O}	9953.35 kJ/kmol
ν_{CO_2}	0.0003 kmol/kmol
e_{ch,CO_2}	20,108.5 kJ/kmol
ν_{Ar}	0.0007 kmol/kmol
$e_{ch,Ar}$	17,998.14 kJ/kmol
e_{ch,H_2}	23,6100 kJ/kmol
P_2	5 bar
η_{cmp}	0.75
η_T	0.85
P_{11}	14 bar
P_{12}	5.3 bar
US_{Loss}	0.05 W/K

The chemical exergy content is generally determined based on two terms as follows. One expresses the energy of formation of the substance's molecule and the other relates to the molar fraction of the reaction products in equilibrium with the environment. The second term is in general negligible with respect to the first. In our calculations we employ fixed values for chemical exergies. Some chemical exergy values of air components are taken from Ref. [36] while the chemical exergy of hydrogen from Ref. [37].

The energy balance at the level of the fuel-cell confirms that the heat generated by the electro-chemical reaction $\dot{Q}_C$ upgrades the enthalpy of the input streams of hydrogen #14 and of air #3 (referring to Fig. 1), and the energy balance for the stack can be written as

$$\dot{m}_{14}h_{14} + \dot{m}_3 h_3 + \dot{Q}_C = \dot{m}_4 h_4 + \dot{Q}_L \tag{3}$$

Here, two streams at the same temperature enter the stack, in #3 and #14, and one stream of oxygen depleted air exits in #4. Taking into account the above-mentioned design criterion as $T_{14} = T_3$, one may assume an average electrolyte temperature as

$$\bar{T}_e = \frac{2T_3 + T_4}{3} \tag{4}$$

The enthalpies in the balance Eq. (3) are estimated as a function of pressure, temperature and the mass concentration of chemical species with the help of the *FluidProp* software [38]. The pressure, temperature and concentration are taken as follows.

The pressure is evaluated starting from the assumed compressor discharge pressure P_2 and by approximating the pressure losses in the heat exchangers so that the exhaust discharges at the atmospheric pressure. It is also assumed that the flow is turbulent, fully developed. Here, compact plate heat exchangers are used. The pressure drop calculations involve a rough estimation the friction coefficient; their corresponding values range between 0.1 and 0.5 bar.

The air composition at state #4 is calculated based on the air composition in the surroundings (through states #1, #2, #3) and the amount of oxygen consumed and water generated, which are:

$$\begin{cases} \dot{m}_{4,O_2} = \dot{m}_{3,O_2} - \dot{m}_{O_{2s}} \\ \dot{m}_{4,H_2O} = \dot{m}_{3,H_2O} + \dot{m}_{H_2O} \end{cases} \tag{5}$$

Based on Eq. (5), the mass concentration of each air compound at state #4 can be calculated:

$$c_i = \frac{\dot{m}_i}{\dot{m}_4}, \quad i = N_2,\ O_2,\ H_2O,\ CO_2,\ Ar \tag{6}$$

The temperatures at states #3 and #4 represent the unknown of the system of Eqs. (3) and (4). The system is solved by an iterative solution method, by guessing a value for T_3, then solving analytically the Eq. (4) for T_4, i.e., $T_4 = 3\bar{T}_e - 2T_3$, evaluating the enthalpies as needed for Eq. (3) and re-iterating for T_3 until the solution of Eq. (3) is found.

Subsequently, the enthalpy, entropy and exergy values of each state point are calculated by assuming the turbine and compressor isentropic efficiencies as listed in Table 2, and hence, assuming that the heat losses from the heat exchangers are negligible as compared to the heat losses at the level of the fuel-cell stack (which is in fact the component where the heat is generated and, therefore, the maximum temperature on the system occurs).

3. System optimization

In the first part of the optimization study, we investigate the impact of system's configuration on its performance. The system

configuration is described here by the amount of volume occupied by the fuel-cell stack from the overall system volume. The system performance is quantified here by two parameters, namely the energy efficiency as

$$\eta = \frac{\dot{W}_C + \dot{W}_T - \dot{W}_{cmp}}{\dot{m}_{11}\mathrm{HHV}} \tag{7}$$

and the volumetric power density as

$$\dot{W}''' = \frac{\dot{W}_C + \dot{W}_T - \dot{W}_{cmp}}{\vartheta_C + \vartheta_{hx}} \tag{8}$$

where HHV is the higher heating value of hydrogen, ϑ_C is the stack volume and ϑ_{hx} represents the volume of the heat exchangers used to preheat the reactants between states #2–3 for air and #12–13–14 for hydrogen (see Fig. 1).

The volume of the fuel-cell stack ϑ_C can be estimated based on the electrolyte membrane thickness, the number of cells and the thickness of the thermal insulation. Here, we first consider a fixed fuel-cell stack volume ϑ_C in the subsequent analysis and vary the volume occupied by the heat exchangers ϑ_{hx}. So, the total volume of the heat exchangers can be simply estimated based on their total energy (heat) capacities:

$$\dot{Q}_{hx} = \dot{Q}_{2-3} + \dot{Q}_{12-13} + \dot{Q}_{13-14} \tag{9}$$

and a compactness factor ϕ is introduced to represent the power density of the heat exchanger as

$$\vartheta_{hx} = \frac{\dot{Q}_{hx}}{\phi} \tag{10}$$

Here, the typical values of ϕ for compact plate-type heat exchangers are expected to range from 100 to 400 kW/m^3, respectively. In the present analysis, we consider 300 kW/m^3 as a common figure and an air stoichiometry of 3, and perform the calculations according to the scheme presented above. As already mentioned, the results regarding the system power density and system efficiency are correlated to the volumetric fraction f, occupied by the fuel-cell stack with respect to the overall system volume as follows:

$$f = \frac{\vartheta_C}{\vartheta_C + \vartheta_{hx}} \tag{11}$$

This will help determine how much the heat exchanger capacity and volume should be for better design, analysis and optimization. In this regard, the results of our calculations are presented in Fig. 3, in terms of variation of the average electrolyte temperature (a) and the power density (b) with f. As the volumetric fraction f increases, both the volume and capacity of the heat exchangers for reactant streams heating decrease. Therefore, the hydrogen and air streams need to be less heated and this reduces the electrolyte temperature as clearly seen from Fig. 3a. As shown in Fig. 3b, one can observe that there is a maximum value of the power density in between these two extreme cases. The first extreme occurs when f becomes low. Then the fuel-cell operates at high temperature and generates high power; however the overall system volume is large, due to the large heat exchangers volumes that occupy the fraction $1-f$ from the overall system. The combination high power/high system volume leads to a low power density.

In the second case one ends up with a large f and thus the heat exchangers having smaller size (capacity) makes the fuel-cell operate at low temperature and hence to generate low power. The combination low power/low system volume leads to low power density. As demonstrated by the results obtained from Fig. 3b, in between the two extreme situations it is found optimum f that maximizes the power density $\dot{W}'''$.

The design problem as illustrated in Fig. 3b can be reformulated in the form of an optimization problem under constraints as follows: find the optimum system configuration that maximizes the power generated per unit of system volume; the system configuration is defined by the parameter f, and the volume of the system, consisting in the stack and heat exchangers, is fixed:

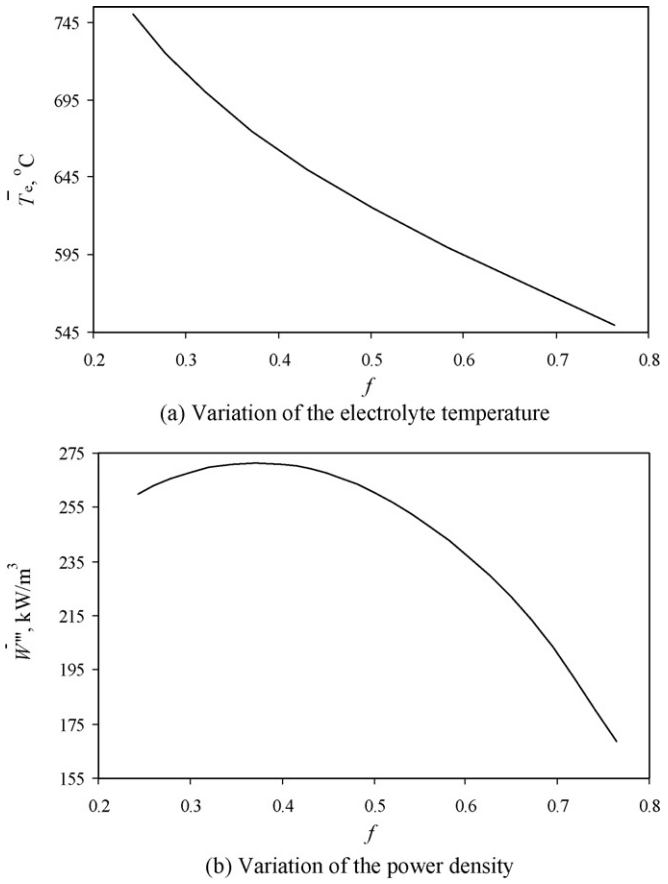

(a) Variation of the electrolyte temperature

(b) Variation of the power density

Fig. 3. The influence of system's configuration f on the operating parameters and performance.

$$\max\{W'''(f),\ \vartheta = \vartheta_C + \vartheta_{hx},\ \text{fixed}\} \tag{12}$$

This is a problem of optimum allocation of resources or kind of constructal design similar to those presented in Bejan's works [39]. For example, in Ref. [40] it is shown that the relative size of systems that function on-board of the vehicles can be derived from the maximization of overall system performance when the optimization process is subjected to technical/economical constraints. In the case of [40] the system weight is constrained because the study refers to an aircraft. In our case, we constrain the system volume because of the type of application. These two approaches (volume-based and weight-based) become equivalent, and one may even study the possibility of constraining both volume and weight to find an optimal design configuration.

This is in fact left for a future analysis, but one may expect that the design is less sensitive to distribution of weight between the stack and heat exchangers provided that one uses compact plate heat exchangers which have the weight per volume ratio in the same range as the fuel-cell stack.

The result of the optimization can be better contemplated in Fig. 4 where both the power density and energy efficiency are plotted on the same graph against the volume fraction f. In order to plot the two curves on the same graph they were normalized with their maximal values. Therefore, one plots the quantities $W^* = \dot{W}'''/\dot{W}'''_{max}$ and $\eta' = \eta/\eta_{max}$ against f. As can be seen in Fig. 4, the system's geometrical configuration, defined by f, affects the performance of the system in terms of both the energy efficiency

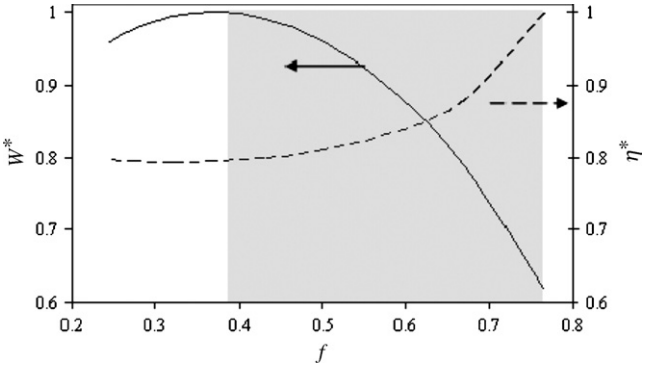

Fig. 4. Variation of the system's power density and energy efficiency with the volumetric fraction occupied by the stack. The quantities are normalized with respect to their maxima.

and power density. As mentioned before, these two parameters are important especially in hydrogen fuelled vehicles that are struggled with the problem of fitting a large hydrogen storage tank on-board and with the problem of maximizing the driving range [1].

The results shown in Fig. 4 suggest that there are two design options for such fuel-cell systems. The first option is to design the system for maximum efficiency. In this case the system configuration is such that f is large, i.e., the fuel-cell stack is large with respect to the other system components (the heat exchangers). For obtaining the maximum efficiency the stack occupies about 75% from the system volume (f is 0.75), as can be read from Fig. 4. The second option is to design the system for maximum power per unit of volume, i.e., for more compactness. In this case the system configuration is such that the stack occupies about 40% from the system's volume while the rest of the system is occupied by the heat exchangers (see Fig. 4). It can also be said that if a system is designed for maximum power generation, it losses efficiency by about 20% out of its maximum efficiency. This is expected to reduce the driving range by the same percent.

In addition, if the system is designed for a maximum energy efficiency to get a maximum driving range with a vehicle, the power density of the system is reduced by about 40% in regards to the system for a maximum power density. Therefore, if this option is chosen, one may end up with less useful space on-board for the system. This is even more clear in Fig. 4 as the gray shaded area for the range of the design parameter f. It apparently ranges in between the two extreme points, i.e., 0.35 and 0.75. It is not feasible to go beyond this range. So, one can consider this as the optimum configuration domain for design.

Furthermore, the minimum threshold of f depends on the adjustment of air stoichiometry. Small air stoichiometry means large f and large power density, while large λ means vice-versa. These aspects

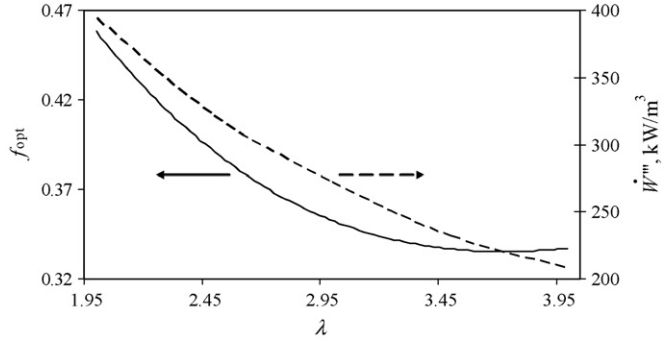

Fig. 5. Optimal volume fraction occupied by the stack and the corresponding maximum power density as a function of the air stoichiometry.

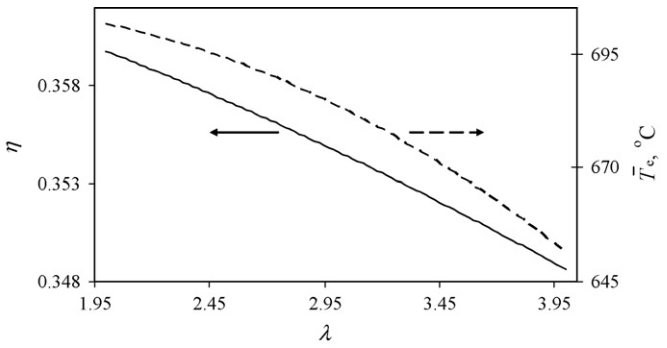

Fig. 6. The energy efficiency and cell's average temperature of the optimized system in function of the air stoichiometry.

can be contemplated from the results presented in Fig. 5. As shown here, the system power density reaches about 400 kW/m^3 for an air stoichiometry of 2, respectively.

4. Parametric study on the optimized system

The energy and exergy efficiencies of the system optimized for a maximum power density are studied for a range of air stoichiometry. The first set of results is presented in Fig. 6 which correlates both energy efficiency and electrolyte temperature with λ. As it can be seen, the efficiency of the optimized system is less influenced by varying the air stoichiometry, while the stack temperature is influenced more drastically. This remains the same if the exergy efficiency is considered instead of energy efficiency. The results regarding various system efficiencies are tabulated in Table 3. The exergy efficiency is generally defined as the useful exergy output divided by the exergy input as

$$\varepsilon = \frac{\dot{W}_c + \dot{W}_T - \dot{W}_{cmp}}{\dot{m}_{11} e_{11} + \dot{m}_1 e_1} \tag{13}$$

Moreover, if the exhaust heat is recovered, the corresponding heat exergy results in

$$\dot{E}_{9-10} = \dot{Q}_{9-10} \left(1 - \frac{T_1}{\bar{T}_{9-10}} \right) \tag{14}$$

and therefore, the system effectiveness including heat recovery then becomes:

$$\varepsilon_{hr} = \frac{\dot{W}_c + \dot{W}_T - \dot{W}_{cmp} + \dot{E}_{9-10}}{\dot{m}_{11} e_{11} + \dot{m}_1 e_1} \tag{15}$$

For calculating the value of ε_{hr} as listed in Table 3 the temperature $\bar{T}_{9-10}$ at which the recovered thermal exergy is delivered is assumed to be with $\Delta T_{9-10} = 10\,^\circ$C less than the average temperature of the hot exhaust stream. This somehow arbitrary value quantifies the average temperature difference between the two streams that exchange heat. The influence of the value of ΔT_{9-10} on the exergy efficiency ε_{hr} is presented in Fig. 7.

The data from Table 3 reveals also that, for the system with heat recovery, the air stoichiometry influences importantly the effectiveness, which varies in the range from 0.61 to 0.74, respectively. These

Table 3
Efficiency and effectiveness of the optimized system.

λ	η (%)	ε	ε_{hr}
2.0	36	0.41	0.74
2.5	36	0.40	0.70
3.0	36	0.40	0.67
3.5	35	0.39	0.64
4.0	35	0.39	0.61

Table 4
Exergy rates for the optimized system with $\lambda = 3$, $f = 0.371$, $S = 1\ m^2$.

Exergy inputs	(W)
11: Fuel	1759
1: Air	79
Total exergy input	1838
Exergy destructions	
1–2: Compressor	53
2–3,7–8: Preheater	86
3–4–14: Fuel cell	337
4–5: Turbine	22
13–14,6–8: Preheater	13
12–13,8–9: Preheater	40
11–12: PresRegulator	24
9–10: HeatRecov	1
Total exergy destruction	575
Exergy outputs	
Turbo-charger	86
10: Exhaust	82
Fuel cell, $\dot{W}_c$	645
$\dot{E}_L = \dot{Q}_L(1 - T_1/T_c)$	22
$\dot{E}_{9-10}$	428
Total exergy output	1263

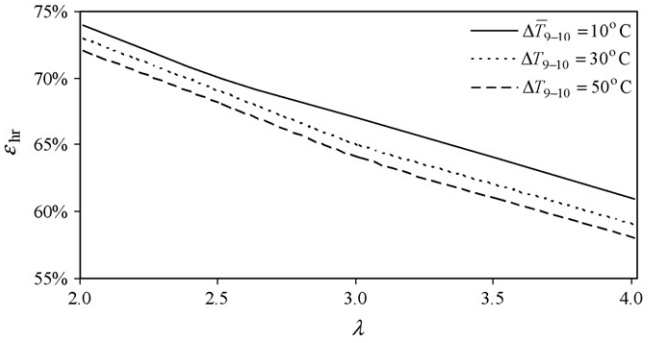

Fig. 7. Variation of the exergy efficiency with the air stoichiometry for several temperature levels at the heat recovery heat exchanger 9–10.

values are rather high, because the exhaust gases can be cooled down to a temperature close to the ambient, as far as none of the environmentally benign substances are contained in them. Moreover, in the cooling process the large heat of condensation of steam may be recovered.

Table 4 tabulates the input and output exergy rates and exergy destruction rates for the various components of the optimized system to achieve the maximum power density. The calculations

Table 5
Various state parameters for the optimized system with $\lambda = 3$, $f = 0.371$.

State 1 intake air		State 6 hydrogen preheater		State 11 state in H_2 tank	
T1	25.0 °C	T6	795.9 °C	T11	25.0 °C
P1	1.01325 bar	P6	1.7132 bar	P11	14 bar
h1	315.229 kJ/kg	h6	1327.1 kJ/kg	h11	3937.316 kJ/kg
s1	6.896 kJ/(kg K)	s6	8.265 kJ/(kg K)	s11	42.532 kJ/(kg K)
e1	52.118 kJ/kg	e6	591.01 kJ/kg	e11	121288.4 kJ/kg
m1	0.00151 kg/s	m6	0.0002 kg/s	m11	1.45E−05 kg/s
H1	0.47628 kW	H6	0.2331 kW	H11	0.057103 kW
E1	0.0787 kW	E6	0.1038 kW	E11	1.759039 kW
State 2 compressor discharge		State 7 Air preheater		State 12 pressure reducer	
T2	250.5 °C	T7	795.9 °C	T12	25.3 °C
P2	5 bar	P7	1.7132 bar	P12	3.7 bar
h2	546.710 kJ/kg	h7	1327.100 kJ/kg	h12	3937.316 kJ/kg
s2	7.012 kJ/(kg K)	s7	8.2649 kJ/(kg K)	s12	48.045 kJ/(kg K)
e2	248.775 kJ/kg	e7	591.01 kJ/kg	e12	119644.6 kJ/kg
m2	0.00151 kg/s	m7	0.0013 kg/s	m12	1.45E−05 kg/s
H2	0.82604 kW	H7	1.7915 kW	H12	0.057103 kW
E2	0.37588 kW	E7	0.7978 kW	E12	1.735199 kW
State 3 preheated air		State 8 exhaust stream		State 13 preheater of H_2	
T3	501.3 °C	T8	546.3 °C	T13	250.6 °C
P3	4.9 bar	P8	1.4132 bar	P13	3.4 bar
h3	816.550 kJ/kg	h8	1025.1 kJ/kg	h13	7195.843 kJ/kg
s3	7.439 kJ/(kg K)	s8	8.001 kJ/(kg K)	s13	56.524 kJ/(kg K)
e3	391.579 kJ/kg	e8	367.56 kJ/kg	e13	120375.1 kJ/kg
m3	0.00151 kg/s	m8	0.0016 kg/s	m13	1.45E−05 kg/s
H3	1.23375 kW	H8	1.5639 kW	H13	0.104361 kW
E3	0.59165 kW	E8	0.5607 kW	E13	1.74579 kW
State 4 fuel-cell outlet		State 9 heat recovery		State 14 hydrogen input	
T4	1022.3 °C	T9	520.0 °C	T14	501.3 °C
P4	4.5 bar	P9	1.2132 bar	P14	3 bar
h4	1612.83 kJ/kg	h9	994.10 kJ/kg	h14	10853.41 kJ/kg
s4	8.217 kJ/(kg K)	s9	8.009 kJ/(kg K)	s14	62.745 kJ/(kg K)
e4	891.083 kJ/kg	e9	334.36 kJ/kg	e14	122177.8 kJ/kg
m4	0.00153 kg/s	m9	0.0015 kg/s	m14	1.45E−05 kg/s
H4	2.46053 kW	H9	1.5166 kW	H14	0.157406 kW
E4	1.35944 kW	E9	0.5101 kW	E14	1.771937 kW
State 5 work recovery		State 10 exhaust gas			
T5	795.9 °C	T10	25.0 °C		
P5	1.71325 bar	P10	1.0132 bar		
h5	1327.09 kJ/kg	h10	282.95 kJ/kg		
s5	8.265 kJ/(kg K)	s10	6.252 kJ/(kg K)		
e5	591.011 kJ/kg	e10	53.502 kJ/kg		
m5	0.00153 kg/s	m10	0.0015 kg/s		
H5	2.02461 kW	H10	0.4317 kW		
E5	0.90165 kW	E10	0.0816 kW		

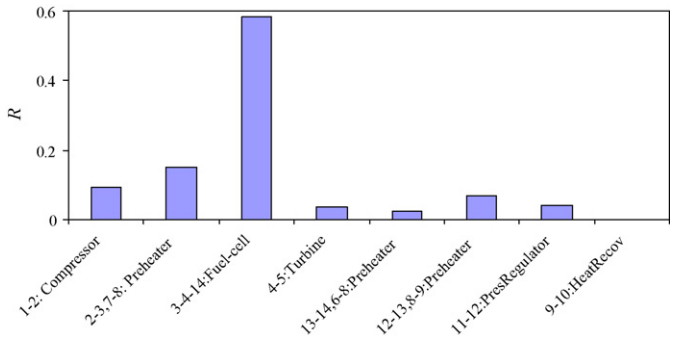

Fig. 8. The exergy destroyed over various system components, reported in percents from the total exergy destroyed.

are done for a unit surface area of the membrane. As expected, the largest exergy destruction takes place in the fuel-cell stack itself which represents about 60% of the total exergy destruction, as shown in Fig. 8 based on the exergy destruction ratio which is introduced in the following form:

$$R = \frac{\dot{E}_{d,i}}{\sum_{k=1}^{N} \dot{E}_{d,k}} \tag{16}$$

where i and k represent the index of the system component (e.g., compressor, heat exchanger, stack, turbine, etc.), and N is the number of system component.

Finally, Table 5 summarizes all state parameters of each flow for the optimized system.

5. Concluding remarks

This study shows that there is an optimal allocation of volumes as occupied by the various components of the SOFC-H^+ system that leads to power maximization per unit of system volume. If more volume is allocated to the heat exchangers the temperature of the preheated gases increases and so does the average cell temperature. Therefore, the cell power density increases. However, the overall volume of the system is large because of the volume occupied by the heat exchangers; thus a decrease in the system power density is induced. If the volume allocated to the heat exchangers is small, the average cell temperature decreases, and so does the power density of the stack; the combination low power and small system volume means low power density. The optimal design configuration, as defined by the volumetric fraction occupied by the stack from the whole system volume, is found in between the two above stated extreme situations.

The optimization principle can be applied for other kinds of high temperature fuel-cell systems, as for example SOFC-O^{2-}, alkaline fuel cells or molten carbonate fuel cells.

The air stoichiometry influences the process in a way that small stoichiometry means both higher power density and efficiency. The energy efficiency is practically not sensitive to air stoichiometry. The exergy efficiency with no heat recovery varies in a narrow range from 39 to 41% for a relatively large range of $\lambda = 2$–4. Almost 60% from the destroyed exergy take place at the level of the fuel-cell itself.

The proton-conducting fuel-cell systems provide an advantage of consuming all hydrogen without a need of afterburner and NO_x emissions. More importantly, SOFC-H^+ systems allow more heat recovery due to steam condensation and exhaust air temperature which is close to the ambient temperature. If heat recovery is considered, the exergy efficiency varies in a large range from 61 to 74%, depending on the air stoichiometry.

The principle of power density maximization through optimal allocation of the volume occupied by each component within the overall system presented herein can be extended to other types of fuel cells. A rational system configuration can be chosen in between the two above discussed options. For a larger driving range, i.e., higher system efficiency, the useful space available on-board will be importantly diminished because the power density is low in this case, whereas for obtaining a large useful space, the driving range will be reduced because the system efficiency is degraded in this case.

Acknowledgements

The authors acknowledge the support provided by the Ontario Premier's Research Excellence Award and the Natural Sciences and Engineering Research Council of Canada.

References

[1] S.O. Mert, I. Dincer, Z. Ozcelik, Exergoeconomic analysis of a vehicular PEM fuel cell system, Journal of Power Sources 165 (2007) 244–252.
[2] S.C. Singhal, K. Kendall, High Temperature Solid Oxide Fuel Cells. Fundamentals, Design and Applications, Elsevier Advanced Technology, Oxford, UK, 2003.
[3] F.J. Gardner, M.J. Day, N.P. Brandon, M.N. Pashley, M. Cassidy, SOFC technology development at Rolls-Royce, Journal of Power Sources 86 (2000) 122–129.
[4] S.H. Chan, C.F. Low, O.L. Ding, Energy and exergy analysis of simple solid oxide fuel-cell power systems, Journal of Power Sources 103 (2002) 188–200.
[5] O.C. Colpan, I. Dincer, F. Hamdullahpur, Thermodynamic modeling of direct internal reforming solid oxide fuel cells operating with syngas, International Journal of Hydrogen Energy 32 (2007) 787–795.
[6] G.J. Saunder, J. Preece, K. Kendall, Formulating liquid hydrocarbon fuels for SOFCs, Journal of Power Sources 131 (2004) 23–26.
[7] A. Wojcik, H. Middleton, I. Damopoulos, J. van Herle, Ammonia as a fuel in solid oxide fuel cells, Journal of Power Sources 118 (2003) 342–348.
[8] Y. Feng, J. Luo, K.T. Chuang, Conversion of propane to propylene in a proton-conducting solid oxide fuel cell, Fuel 86 (2007) 123–128.
[9] W. Winkler, H. Lorenz, Design studies of mobile applications with SOFC-heat engine modules, Journal of Power Sources 106 (2002) 338–343.
[10] A.L. Dicks, R.G. Fellows, C. Martin Mescal, C. Seymour, A study of SOFC–PEM hybrid systems, Journal of Power Sources 86 (2000) 501–506.
[11] C.O. Colpan, I. Dincer, F. Hamdullahpur, A review on macro-level modeling of planar solid oxide fuel cells, International Journal of Energy Research 32 (2008) 336–355.
[12] M.M. Hussain, X. Li, I. Dincer, Mathematical modeling of planar solid oxide fuel cells, Journal of Power Sources 161 (2006) 1012–1022.
[13] J. Palsson, A. Selimovic, L. Sjunnesson, Combined solid oxide fuel cell and gas turbine systems for efficient power and heat generation, Journal of Power Sources 86 (2000) 442–448.
[14] M. Granovskii, I. Dincer, M.A. Rosen, Performance comparison of two combined SOFC–gas turbine systems, Journal of Power Sources 165 (2007) 307–314.
[15] P. Ranran, W. Yan, Y. Lizhai, M. Zongqiang, Electrochemical properties of intermediate-temperature SOFCs based on proton conducting Sm-doped $BaCeO_3$ electrolyte thin film, Solid State Ionics 177 (2006) 389–393.
[16] W. Jamsak, S. Assabumrungrat, P.L. Douglas, N. Laosiripojana, S. Charojrochkul, Theoretical performance analysis of ethanol-fuelled solid oxide fuel cells with different electrolytes, Chemical Engineering Journal 119 (2006) 11–18.
[17] A. Demin, P. Tsiakaras, Thermodynamic analysis of a hydrogen fed solid oxide fuel cell based on a proton conductor, International Journal of Hydrogen Energy 26 (2001) 1103–1108.
[18] G.B. Goodenough, Oxide-ion electrolytes, Annual Review of Materials Research 33 (2003) 91–128.
[19] Z. Zhan, S.A. Barnett, Use of a catalyst layer for propane partial oxidation in solid oxide fuel cells, Solid State Ionics 176 (2005) 871–879.
[20] K.D. Kreuer, Proton-conducting oxides, Annual Review of Materials Research 33 (2003) 333–359.
[21] S. Assabumrungrat, N. Laosiripojana, V. Pavarajarn, W. Sangtongkitcharoen, A. Tangjitmatee, P. Praserthdam, Thermodynamic analysis of carbon formation in a solid oxide fuel cell with a direct internal reformer fuelled by methanol, Journal of Power Sources 139 (2005) 55–60.
[22] S. Assabumrungrat, W. Sangtongkitcharoen, N. Laosiripojana, A. Arpornwichanop, S. Charojrochkul, P. Praserthdam, Effects of electrolyte type and flow pattern on performance of methanol-fuelled solid oxide fuel cells, Journal of Power Sources 148 (2005) 18–23.
[23] S. Assabumrungrat, V. Pavarajarn, S. Charojrochkul, N. Laosiripojana, Thermodynamic analysis for a solid oxide fuel cell with direct internal reforming fueled by ethanol, Chemical Engineering Science 59 (2004) 6015–6020.
[24] W. Sangtongkitcharoen, S. Assabumrungrat, V. Pavarajarn, N. Laosiripojana, P. Praserthdam, Comparison of carbon formation boundary in different modes of solid oxide fuel cells fueled by methane, Journal of Power Sources 142 (2005) 75–80.

[25] N. Maffei, L. Pelletier, J.P. Charland, A. McFarlan, A direct ammonia fuel cell using bariumcerate proton conducting electrolyte doped with gadolinium and praseodymium, Fuel Cells 07 (4) (2007) 323–328.
[26] M. Ni, M.K.H. Leung, D.Y.C. Leung, Mathematical modeling of proton-conducting solid oxide fuel cells and comparison with oxygen-ion-conducting counterpart, Fuel Cells 07 (4) (2007) 269–278.
[27] M. Ni, M.K.H. Leung, D.Y.C. Leung, Electrochemical modeling of hydrogen production by proton-conducting solid oxide steam electrolyzer, International Journal of Hydrogen energy 33 (2008) 4040–4047.
[28] I. Dincer, M.A. Rosen, Exergy, Elsevier Science, London, 2007, pp. 500.
[29] M. Ay, A. Midilli, I. Dincer, Thermodynamic modeling of a proton exchange membrane fuel cell, International Journal of Exergy 3 (1) (2006).
[30] K.W. Bedringas, T.I.S. Ertesvag, S. Byggstoyl, B.F. Magnussen, Exergy analysis of solid-oxide fuel-cell (SOFC) systems, Energy 22 (4) (1997) 403–412.
[31] A. Mawardi, F. Yang, R. Pitchumani, Optimization of the operating parameters of a proton exchange membrane fuel cell for maximum power density, Journal of Fuel Cell Science and Technology 2 (2005) 121–135.
[32] J.V.C. Vargas, J.C. Ordonez, A. Bejan, Constructal flow structure for a PEM fuel cell, International Journal of Heat and Mass transfer 47 (2004) 4177–4193.
[33] J.V.C. Vargas, J.C. Ordonez, A. Bejan, Constructal PEM fuel cell stack design, International Journal of Heat and Mass Transfer 48 (2004) 4410–4427.
[34] C. Chen, X. Li, T. Wang, X. Zhang, J. Li, P. Dong, D. Zheng, B. Xia, A self-breathing proton-exchange-membrane fuel-cell pack with optimal design and microfabrication, Journal of Microelectromechanical Systems 15 (2006) 1088–1097.
[35] J. Larminie, A. Dicks, Fuel-cell Systems Explained, 2nd Edition, John Wiley and Sons, Chichester, UK, 2003, pp. 418.
[36] M.M. Hussain, J.J. Baschuk, X. Li, I. Dincer, Thermodynamic analysis of a PEM fuel-cell power system, International Journal of Thermal Sciences 44 (2005) 903–911.
[37] T.L. Woods, R.M. Garrels, Thermodynamic Values at Low Temperature for Natural Inorganic Materials: An Uncritical Summary, Oxford University Press, NY, 1987, pp. 242.
[38] P. Colonna, T.P. van der Stelt, FluidProp: a program for the estimation of thermo physical properties of fluids, Energy Technology Section, Delft University of Technology, 2004, The Netherlands (www.FluidProp.com).
[39] A. Bejan, Shape and Structure, from Engineering to Nature, Cambridge University Press, Cambridge, UK, 2000, pp. 343.
[40] J.C. Ordóñez, A. Bejan, System-level optimization of the sizes of organs for heat and fluid flow systems, International Journal of Thermal Sciences 42 (2003) 335–342.